



Wearable, battery-free, wireless multiplexed printed sensors for heat stroke prevention with mussel-inspired bio-adhesive membranes

Gabriel Maroli^{a,b}, Giulio Rosati^{a,**}, Salvio Suárez-García^{a,***}, Daniel Bedmar-Romero^a, Robert Kobrin^{a,c}, Álvaro González-Laredo^a, Massimo Urban^a, Ruslan Álvarez-Diduk^a, Daniel Ruiz-Molina^a, Arben Merkoçi^{a,d,*}

^a Catalan Institute of Nanoscience and Nanotechnology, BIST, and CSIC, Edifici ICN2 Campus UAB, 08193, Bellaterra, Barcelona, Spain

^b Instituto de Investigaciones en Ingeniería Eléctrica Alfredo Desages (IIIE), Universidad Nacional del Sur – CONICET, Argentina

^c Joint Department of Biomedical Engineering, NC State & UNC Chapel Hill, USA

^d Catalan Institution for Research and Advanced Studies (ICREA), Passeig de Lluís Companys, 23, Barcelona, 08010, Spain

ARTICLE INFO

Keywords:

Inkjet printing
Bio-adhesive membranes
Heat stroke
NFC
Silver nanoparticles
Wearables

ABSTRACT

Wearable technologies are becoming pervasive in our society, and their development continues to accelerate the untapped potential of continuous and ubiquitous sensing, coupled with big data analysis and interpretation, has only just begun to unfold. However, existing wearable devices are still bulky (mainly due to batteries and electronics) and have suboptimal skin contact. In this work, we propose a novel approach based on a sensor network produced through inkjet printing of nanofunctional inks onto a semipermeable substrate. This network enables real-time monitoring of critical physiological parameters, including temperature, humidity, and muscle contraction. Remarkably, our system operates under battery-free and wireless near-field communication (NFC) technology for data readout via smartphones. Moreover, two of the three sensors were integrated onto a naturally adhesive bioinspired membrane. This membrane, developed using an eco-friendly, high-throughput process, draws inspiration from the remarkable adhesive properties of mussel-inspired molecules. The resulting ultra-conformable membrane adheres effortlessly to the skin, ensuring reliable and continuous data collection. The urgency of effective monitoring systems cannot be overstated, especially in the context of rising heat stroke incidents attributed to climate change and high-risk occupations. Heat stroke manifests as elevated skin temperature, lack of sweating, and seizures. Swift intervention is crucial to prevent progression to coma or fatality. Therefore, our proposed system holds immense promise for the monitoring of these parameters on the field, benefiting both the general population and high-risk workers, such as firefighters.

1. Introduction

Heat stroke, a life-threatening condition, manifests in two distinct forms: classic heat stroke (CHS), due to passive heat exposure, and exertional heat stroke (EHS), linked to physical activity. CHS occurs at rest and affects mostly vulnerable populations, such as children left in sun-exposed closed vehicles and elderly populations during heat waves. On the other hand, EHS strikes athletes (both elite and recreational), military personnel, and individuals engaged in physically demanding occupations, often in hot environments. Moreover, EHS is characterized by significant central nervous system (CNS) dysfunction, hyperthermia,

and organ/tissue damage (Laitano et al., 2019). When the CNS succumbs to temperatures exceeding 40.5 °C, symptoms escalate rapidly (Al Mahri and Bouchama, 2018). In this scenario, prompt diagnosis is crucial for offering an effective treatment, starting with lowering the patient's temperature and alerting the healthcare emergency system (McEntire et al., 2013; Kim et al., 2019). In a world facing escalating temperatures, especially during intense summers, wearable monitoring systems emerge as critical allies. Wearable devices have become ubiquitous, yet their sensor technologies often face sensor instability requiring frequent replacements. On the other side, electrochemical or electrical sensing, known for their direct, sensitive detection and cost-effectiveness, hold

* Corresponding author. Catalan Institute of Nanoscience and Nanotechnology, BIST, and CSIC, Edifici ICN2 Campus UAB, 08193, Bellaterra, Barcelona, Spain.

** Corresponding author.

*** Corresponding author.

E-mail addresses: giulio.rosati@icn2.cat (G. Rosati), salvio.suarez@icn2.cat (S. Suárez-García), arben.merkoci@icn2.cat (A. Merkoçi).

immense promise for targeted diagnostics and monitoring. These systems empower currently existing prevention mechanisms, enabling early alerts and rapid responses. In this context, a compelling use case is heat stroke prevention, crucial for the general public and high-intensity workers, such as firefighters.

Several pioneering efforts have aimed at early detection of heat stroke, yielding a spectrum of sensor-based solutions. In this sense, Momose et al., (2023) proposed an information system for EHS prevention based on a simple sweat ratemeter only. In the work of Chen et al., (2017) a multiparameter (multi-sensor) system analyzing galvanic skin response (GSR), body temperature, sweat, and heart rate was introduced. However, the system is battery-based, bulky, wired, and uncomfortable to wear. In a similar study, Pham et al., (2020) worked on the ongoing challenges of achieving an optimal balance between wearability and functionality but without managing a strong integration. Other interesting approaches to EHS and CHS prevention have focused on machine learning for an in-depth analysis of the vital signs (Shimazaki et al., 2022). Despite granting high stability, these bulky electronic components compromise the usability of the system during routine operations by workers or everyday life by individuals. A notable breakthrough came in the form of an earbud-type wearable system (Matsumoto et al., 2019). Equipped with temperature and sweat sensors, this system demonstrated promising results.

To devise a sensitive and precise heat stroke detection system, it's crucial to align symptoms with measurable skin values. The CDC website lists the following as the main symptoms of heat stroke: confusion, loss of consciousness, hot dry skin or profuse sweating, seizures, very high body temperature, death if treatment delayed. Of these, the first two are not related to physiological conditions. The third, the fourth, and the fifth are measurable with our device thanks to humidity sensing (both in the case of no sweating, i.e. low humidity and profuse sweating, i.e. high humidity), muscles contraction, and skin temperature sensing. For temperature sensing, one of the most common approaches requiring just a conductor is the use of a "meander" resistor (Ershad et al., 2020), which resistance varies with temperature due to mechanical dilation. For humidity sensing, interdigitated electrodes (IDE) are typically used in combination with a permeable membrane trapping humidity and therefore changing its dielectric properties (Barmpakos et al., 2020), such as resistance and capacitance. Regarding seizures detection with sEMG, (Baumgartner et al., 2021) proved that sEMG single channel measurements can be used to accurately identify seizures in epilepsy, extending the work of Conradsen et al., (2011). Djemal et al. also push forward the concept in 2023 (Djemal et al., 2023) using wearable (despite bulky and battery-based) single channel sensors with the same aim and proving their accuracy for the seizures detection. SEMG and muscle contraction can be easily measured as well simply using a couple of electrodes accurately placed along the muscle direction and measuring the action potential crossing them (Rosati et al., 2021). However, for these sensors to thrive in wearable applications, they must overcome connectivity challenges (power, readout, and connection to smartphones or other portable devices). Most published works showcase visually appealing devices but omit details on amplifier connections and data analyzers (often wired). Some progress includes wireless data transmission protocols, but these typically bulky modules require power sources like batteries or energy harvesters. The typical wireless data transmission protocols used for this purpose are (in descending order of power consumption and distance reached): wi-fi, low-power Bluetooth (Yang et al., 2022; Zhao et al., 2023), and near field communication (NFC). Notably, NFC does not need external power (i.e. batteries) as the reader powers the system through the data-reading antenna (Haerinia and Noghianian, 2019; Rossetti et al., 2024), for more details of the NFC functionality check the Supplementary Information.

Among techniques for fabricating battery-free wireless data transmission systems on flexible 2D substrates, printing emerges as a stand-out for its performance and features. Nanofunctional inks based on cost-effective silver nanoparticles can form highly conductive paths, allowing

for the fabrication of electronic circuits, sensors, and antennas by inkjet printing (Yang et al., 2022; Maroli et al., 2023; Nalepa et al., 2024). Even consumer printers can be adapted for these applications, yielding low-cost, scalable disposable devices on plastic substrates (Rosati et al., 2022). While inkjet printing surpasses screen printing in terms of being maskless and wasteless, it may face issues like poor adhesion to the substrate and often requires post-treatments. Besides, the thinness of inkjet-printed layers (typically less than 1 μm) can affect conductivity and durability. On the other hand, hybrid contactless printing techniques like the one proposed by Voltera allow for on-demand deposition of conductive pastes by syringe-based deposition, making it suitable for fragile substrates.

In wearable technologies, the first crucial step is ensuring intimate skin-sensor contact. While various technologies address heat stroke symptom detection, the adhesive system that secures wearables to the skin remains pivotal. An innovative approach involves nature-inspired bioadhesive membranes, drawing inspiration from mussel-like materials widely used in biomedical applications (Barros et al., 2021). Observing the remarkable functions that characterize these living organisms (e.g., underwater adhesion), research has been focused on imitating those functions. Over the past years, it has been determined that catecholamine-based molecules are playing a crucial role in the chemical structure of adhesive proteins (Lee et al., 2006), leading to the development of synthetic materials through catecholamine polymerization (dopamine-like polymers). These catechol groups and polyphenolic molecules provide adhesive properties across a wide variety of surfaces even in aqueous environments (Saiz-Poseu et al., 2019), tissues (Ju et al., 2022) and skin (Sousa et al., 2018). When polymerized with amino-based ligands, the resulting membranes offer chemical versatility, high biocompatibility, and crucial skin conformability (Contreras-Pereda et al., 2024). Thus, these membranes serve a dual role: maintaining close skin contact for 2D flexible devices and acting as a platform for integrating electronic circuits and sensors via out-of-the-cleanroom and non-contact additive manufacturing techniques.

Hence, in this work, we explored the development of printed sensors on a polyethylene terephthalate (PET) with a semipermeable coating, and on nature-inspired membranes (Fig. 1). The aim was to create integrated circuits and NFC antennas for battery-free and wireless readout of a network of critical sensors crucial in heat stroke prevention (temperature, humidity and muscle contraction). The adhesive membrane was designed, drawing inspiration from mussel adhesion molecules. Commercially available reagents (pyrocatechol and hexamethylenediamine) were used, and their polymerization yielded structures inspired to those observed in mussels. We examined two integration approaches: integrating sensor circuits on the PET substrate with interconnected antennas and using the membranes to maintain skin contact, and alternatively, direct sensor and antenna printing onto the adhesive membranes. The advantages and disadvantages of inkjet printing and paste deposition using a Voltera printer were also evaluated. Finally, the whole platform has been validated both in a controlled lab environment and through *in vivo* testing on healthy volunteers during physical activity.

2. Materials and methods

2.1. Membranes fabrication and characterization

All reagents were purchased and used without further purification from Sigma-Aldrich (Madrid, Spain). Solvents were used as received without additional drying or degassing (Scharlab, Madrid, Spain). Type 1 ultrapure water from in-house Milli-Q® filtration systems (Millipore, Burlington, MA) was used in all experiments unless otherwise specified.

The synthesis of the bioinspired membranes was performed following the previously reported protocol (Contreras-Pereda et al., 2024) with the following modifications: the catechol-based molecule

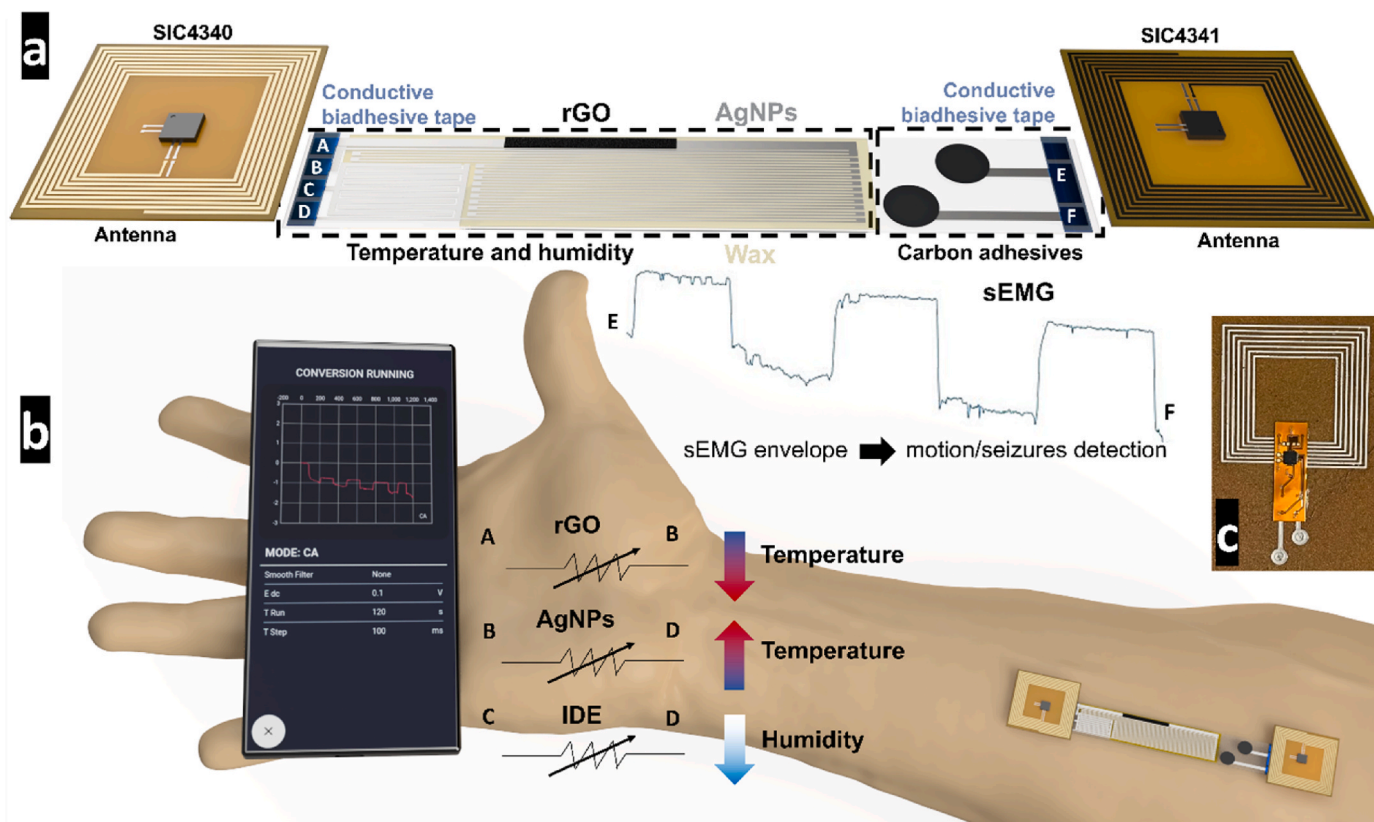


Fig. 1. a) Schematic of the sensor network. The rGO temperature sensor is connected between pads A and B and exhibits a decrease in resistance value with increasing temperature, as indicated by the arrows. The silver sensor between pads B and D exhibits an increase in resistance value with increasing temperature. The humidity sensor, consisting of a silver interdigitate, between pads C and D evaluates the change in conductivity of the substrate. As the humidity increases, the resistance decreases. The electrodes used for motion and seizure detection are located between pads E and F. b) Schematic of the sensor placement on the forearm. c) Picture of the electrodes and antenna directly printed on the bioadhesive membrane with the NFC chip.

used was benzene-1,2-diol (pyrocatechol, 10 mmol) and mixed with hexamethylenediamine (HMDA, 10 mmol).

Hyperion 2000 FTIR microscope (Bruker Optik, GmbH, Ettlingen, Germany) was used in reflection mode, which is equipped with a nitrogen-cooled mercury-cadmium-telluride (MCT) detector (Infrared Associates, Inc., Stuart, FL, USA) using a $15\times$ reflection objective, a gold mirror as reference and scanning for 30 min with a resolution of 4 cm^{-1} . For the analysis, the membranes were attached to a gold surface. All the data obtained was processed using the Opus version 7.2.139.1294 (Bruker) software.

Cell viability assay was performed using PrestoBlue™ cell viability kit (Invitrogen™) to evaluate the possible cytotoxic effects of the membranes in the NIH/3T3 cell line. Initially, a total of 5×10^4 cells/well with 100 μl medium were seeded in a 96-well plate (Falcon™ 353072, Fisher Scientific) and incubated at 37°C for 24 h. Cells without membranes were used as controls, while membranes (cut in circular discs of 8 mm in diameter and UV sterilized) were incorporated into each well, followed by incubation at 37°C for 24 h. Afterward, the membranes and medium were removed and 10 μl of PrestoBlue™ cell viability kit were added to each well following the manufacturer specifications and finally read (Victor3, PerkinElmer). In each plate, three replicates were done for each condition and a total of four repetitions ($N = 4$) were performed. Results were represented with OriginPro version 9.8.0.200 software.

Images obtained from SEM measurements were acquired on a scanning electron microscope (FEI Quanta 650 FEG, Thermo Fisher Scientific, Eindhoven, The Netherlands) in secondary electron mode with a beam voltage between 2 and 20 kV and chamber pressure of 10^{-5} Pa. The working distance was set at 10 mm and different amplifications

were tested for final images. The samples were prepared by attaching the membranes on aluminum stubs. Before performing the analysis, the samples were metalized by depositing on the surface a thin Pt coating (5 nm) using a sputter coater (Leica EM ACE600).

2.2. Sensors network printing and stamping

For inkjet-printed devices, a commercial silver ink (Mitsubishi Paper Mills Silver Nano™ AgNP, NBSIJMU01) was loaded into a rechargeable cartridge and printed with an Epson XP15000 printer on the Mitsubishi Paper Mills special substrate (NB-TP-3GU100) and on the membrane as further detailed later. For the deposition of the screen printing pastes, the V-one dispenser/printer from Voltera (Canada) was used. The pastes Flex 2, Lot: GigglingGrouper and solder Paste T5, Lot: IcyInchworm, were purchased from Voltera. Flexible polyamide PCBs were fabricated by PCBWay, China. The 3M Electrically Conductive Adhesive Transfer Tape 9703 was purchased in Digikey. For the reduced graphene oxide (rGO) temperature sensor, Graphene oxide (GO) dispersions (1 wt%) were purchased from Graphenea (Spain). All reagents for the saturated solution (LiCl , MgCl_2 , KCO_3 , NaNO_3 , NaCl , KCl , KNO_3) were purchased and used without further purification from Sigma-Aldrich. The digital multimeter Keithley DMM6500 was purchased in Farnell Components SL. The carbon conductive adhesives tabs 16084-1 tabs 16084-1 were purchased in Ted Pella, Inc.

For the fabrication of the sensor network on the Mitsubishi substrate, the silver trace layout was first printed twice with the Epson printer. This approach aimed to enhance conductivity by incorporating a higher volume of silver nanoparticles within the ink. In parallel, the Graphene Oxide (GO) was filtered and subsequently reduced by laser following the

steps previously reported (Scroccarello, 2023). Then, the trace of reduced Graphene Oxide (rGO) was transferred to the substrate by a press. Next, the carbon conductive adhesive tabs were placed on the silver circles reserved to be the electrodes. Finally, using 3M 9703 conductive tape, the flexible PCBs were attached to the connection pads. The fabrication steps can be seen in Fig. 2.

2.3. Smartphone readout

Near Field Communication (NFC) technology is a short-distance communication protocol, in the order of 5 cm, that operates at 13.56 MHz on ISO/IEC 18000-3 air interface and at rates ranging from 106 kbit/s to 424 kbit/s. NFC uses loop antennas, whose inductance value will be determined by the internal capacity of the chip to be used, in such a way that the resonance frequency between the designed antenna and the internal capacitor is 13.56 MHz. It is also possible to incorporate external capacitors to reduce the value of the desired inductance. In addition, the parasitic capacitance presented by the inductor must be taken into account. A compact model of the concentrated components of the inductor and the capacitance of the chip can be seen in Fig. S1. Based on this model, the resonance frequency of the antenna and chip set will be given by,

$$f_{\text{resonance}} = \frac{1}{2\pi\sqrt{L(C_{\text{chip}} + C_{\text{parasitic}})}} \quad (\text{Eq. 1})$$

Most of the chips for NFC communication have an internal capacitance of the order of 50 pF, and thus this will be the starting point for the design of the inductor. In particular, the chip used in this work from Silicon Craft has an internal capacitance of 51 pF. Using Eq. (1), and neglecting the parasitic capacitance of the inductor, the required inductance value will be calculated. With the inductance value determined, the inductor is designed geometrically (Maroli et al, 2021), the parasitic capacitance is obtained and the model is iteratively adjusted. As the first iteration step, the required inductance will be $L = 1/(2\pi f_{\text{res}})^2 C_{\text{chip}} = 2.75 \mu\text{H}$. Another important parameter to take into account in this type of design is the series resistance that the inductor will have. Both its length, as well as the width and thickness of the traces will determine the resistance value. This parameter is very important as it will define the quality factor (Q) of the inductor, where $Q = \omega L/R$. The quality factor is entirely related to the distance at which our antenna will be able to transmit. This relationship can be seen in Ortego's work.

The SIC4340 integrated circuit, developed by Silicon Craft, exhibits remarkable versatility in its ability to measure resistance across a wide

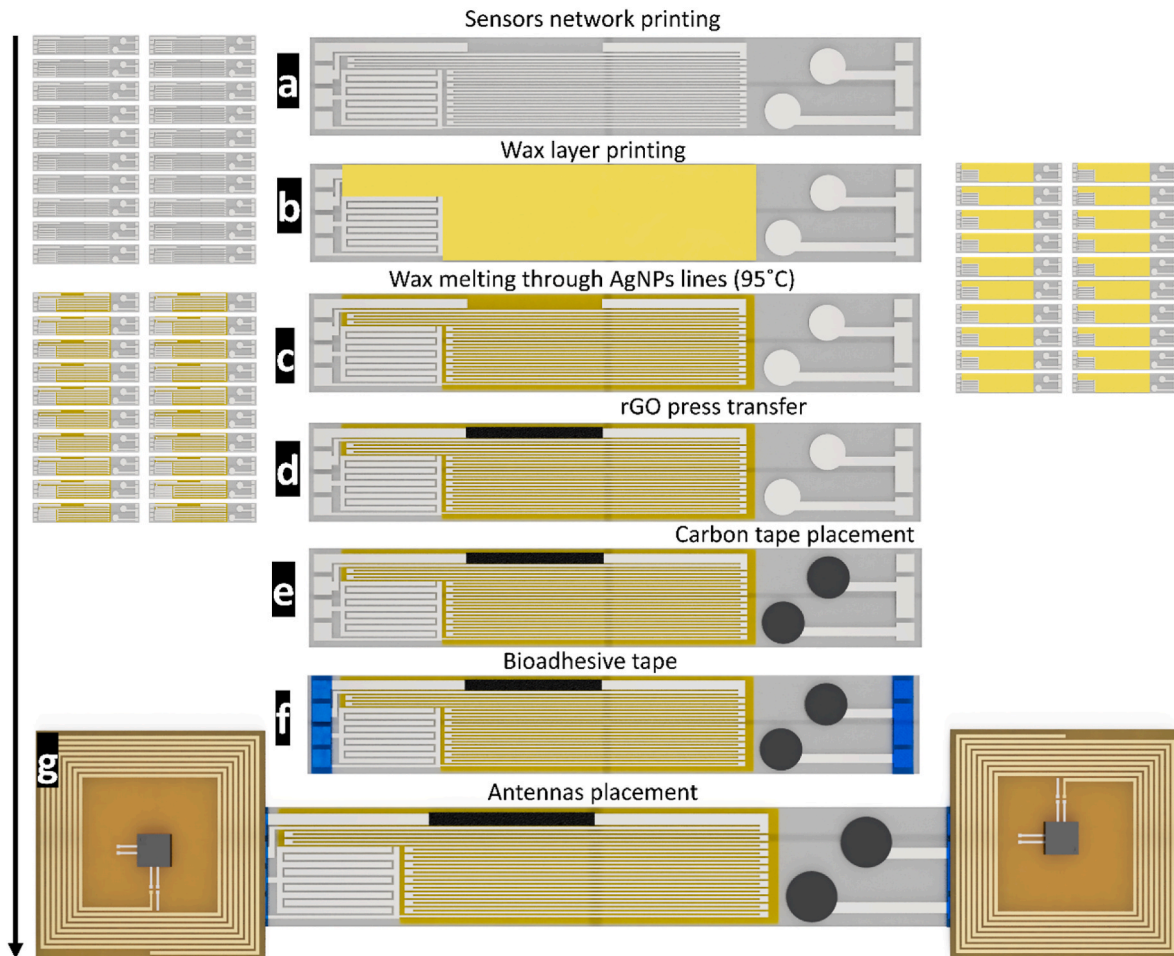


Fig. 2. Represented from top to bottom the fabrication steps of the inkjet-printed sensors network on Mitsubishi semi-permeable substrate and of its preparation for the temperature, humidity and simplified surface electromyography (ssEMG), measurements with the near-field communication (NFC) antennas. a) The sensor network is printed on the A4-sized Mitsubishi substrate. To enhance the conductivity of the traces, the design is printed twice. b) The wax printer is then employed to print a coating of wax, which adheres to the substrate and the silver traces. This step is also carried out in duplicate. c) To allow the wax to permeate the substrate and to remove it from the silver traces, the sensor is passed through a laminator, covering the devices with a sheet of paper. The wax diffuses into the substrate, and any excess is absorbed by the paper. d) In this step, the devices are cut and manipulated one by one. The reduced Graphene Oxide (rGO) sensor, previously reduced by laser, is transferred using a press. e) Carbon tape circles are placed on the printed electrodes. f) Anisotropic conductive tape is placed on the connection pads between the antennas and the device. g) Finally, the antennas are connected to the device.

spectrum. To ensure accurate measurements, it is essential to configure the bias current such that the voltage readings acquired by the chip fall within the range of 0.2 V–1.2 V. The resistance value can be derived using the formula $R = V_{sen}/I_{sen}$, where I_{sen} represents the bias current,

which can be adjusted within the range of 1 μ A–504 μ A. However, it is important to note that setting the bias current below 10 μ A may introduce significant errors, primarily attributed to the least significant bit (LSB). Consequently, we consider the valid range of current to be 10

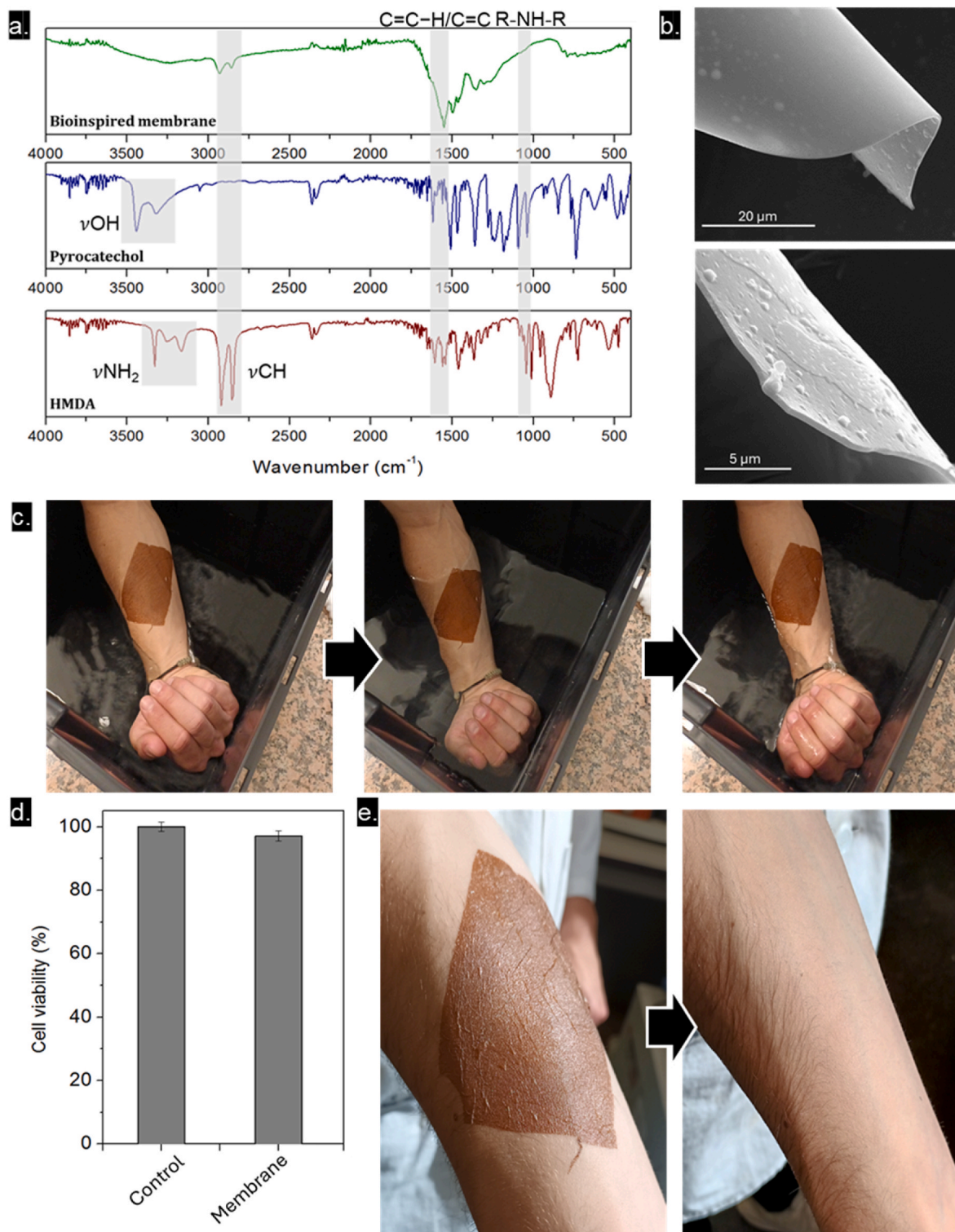


Fig. 3. Bioinspired membranes were characterized after their synthesis to corroborate the correct polymerization, adhesion and biocompatibility. a) FT-IR spectroscopy measurements corroborated the polymerization between pyrocatechol and hexamethylenediamine (HMDA) ligands for the formation of the membranes. b) Scanning electron microscopy (SEM) showed the formation of thin free-standing membranes. c) Water-resistant adhesion was demonstrated by subsequent cycles of water immersion of a membrane adhered directly to the skin of a volunteer. d) *In vitro* biocompatibility was studied in fibroblast cells (NIH/3T3), showing high cell viability, thus demonstrating the low toxicity of the membranes. e) The membrane conformability to the skin was excellent, ensuring intimate contact between the tissue and the device, which can be easily removed if needed without inducing any skin damage.

μA –504 μA , paired with a voltage range of 0.2 V–1.2 V.

Taking these constraints into account, we can establish the lower and upper resistance limits as follows: $R_{\text{min}} = 0.2\text{V}/500 \mu\text{A} = 400 \Omega$ and $R_{\text{max}} = 1.2\text{V}/10 \mu\text{A} = 120 \text{K}\Omega$. This affords us the capability to detect resistance variations up to 300-fold when adapting the bias current for each measurement. Conversely, if the bias current remains fixed, the detectable variation is limited to a factor of 6.

Furthermore, it is noteworthy that the SIC4340 Chip features three channels. This allows for the adaptation of bias current values to create three distinct measurement ranges, thereby expanding the range of detectable variations to 216 times.

For muscle contraction measurements, simplified surface electromyography (ssEMG), the SIC4341 integrated circuit, also from Silicon Craft, was used. This integrated circuit is intended for electrochemical measurements, but since it can perform chronoamperometry, it is suitable for this application. Like a potentiostat, the chip has a connection for 3 electrodes, Working, Counter and Reference. However, the smartphone application provided by the manufacturer, gives the possibility to configure the system on 2 electrodes, only considering the Working and the Counter. This was the mode selected for the muscle contraction measurements. A voltage of 0.5 V, a run time of 300 s and a measurement interval of 100 ms were configured. To improve the connection between the printed pads and the skin, carbon conductive adhesive tabs were used. For the larger muscles such as the bicep and tricep, the scale of 20 μA was used, while for finger movement recording the scale selected was 2.5 μA .

3. Results and discussion

3.1. Membranes characterization

The membranes were synthesized following a straightforward methodology which allows for the formation of a bioinspired material based on catecholamines that imitates some of the properties found in mussels. In this case, pyrocatechol and HMDA ligands, which are commercially available, were used for their polymerization, obtaining a polydopamine-like structure inspired to those observed in mussels (Suárez-García et al., 2017). The analysis of the FT-IR spectra (Fig. 3a) corroborated the polymerization of the membrane. The broad band around 3250 cm^{-1} , corresponded to the stretching vibrations of hydroxyl ($-\text{OH}$) and amine ($-\text{NH}_2$) groups, whose peaks can be appreciated in the catechol derivatives and HMDA spectra, respectively. The peaks around 2850 cm^{-1} could be attributed to asymmetric and symmetric stretching vibrations of aliphatic carbons ($\text{C}-\text{H}$) of HMDA. The peak at 1700 cm^{-1} corresponds to quinones ($\text{C}=\text{O}$). Finally, the signal around 1500 cm^{-1} was attributed to $\text{C}=\text{C}-\text{H}$ and $\text{C}=\text{C}$ vibrations from the catecholic/quinonic rings of the catechol derivatives, while the peak at 1260 cm^{-1} belongs to a secondary amine binding an alkyl or an aromatic ring.

Besides, the SEM analysis of the membrane showed a sub-micrometer uniform thickness and a relatively flat surface (Fig. 3b). These morphological properties endow the membranes with ultra-conformable adaptability to the skin (Fig. 3c–e). Interestingly, the membranes showed great adhesion on the skin mainly due to the chemical structure previously discussed. The water-resistant adhesion was corroborated by immersing a membrane attached to the skin of a volunteer for severe cycles (Fig. 3c). The bioadhesive membrane developed allows for the direct adhesion of the device onto the skin, meeting two of the main requirements: i) it is capable of keeping the device in place for the required time, even in conditions of humidity and movement, and ii) it can be easily removed without causing pain or injury to the skin (Supplementary Information videos SV1). The needed adhesion is a compromise between resistance and adhesive capacity on the skin, as high adhesion could limit its application due to skin damage. In our case, we have achieved a balance by obtaining sufficient adhesion that allows the device to be supported on the skin in

conditions of movement and humidity but that can also be easily removed at any time.

Finally, the *in vitro* biocompatibility of the membranes was corroborated, showing cell viability above 95% in fibroblast cells (Fig. 3d and Fig. S2). Similarly, the tests performed directly on *in vivo* skin have shown a high biocompatibility of the material without showing signs of inflammation, irritation, or erythema on the skin where the adhesive membrane was applied (Fig. 3e). As previously mentioned, the conformability of the membrane on the skin was excellent, perfectly adapting to the relief of the skin and facilitating the intimate adherence between the tissue and the membrane without causing any injury (Fig. 3e).

3.2. Humidity and temperature double sensing

In our research endeavor, we harnessed the capabilities of the SIC-4340 chip, which boasts three measuring channels. Within this framework, we strategically deployed three sensors: a humidity sensor alongside two temperature sensors, one with a negative coefficient and the other with a positive coefficient. The humidity sensor consists of an IDE sensor. Unlike conventional capacitance-based measurements, we focus on the resistance change of the Mitsubishi substrate as it absorbs humidity. To characterize this sensor, the IDEs were placed inside a plastic beaker, maintaining constant relative humidity as shown in Fig. S3. For that, saturated solutions of different salts (LiCl (11%), MgCl_2 (33%), KCO_3 (43%), NaNO_3 (64%), NaCl (75%), KCl (84%) and KNO_3 (94%)) were prepared. The resulting resistance changes were measured with a digital multimeter. Notably, the linear region of the calibration curve emerged at 11% RH and 33% RH, yielding resistance values exceeding 100 MOhm and 43 MOhm, respectively (Fig. 4a). At 94% RH, the sensor reached saturation, indicating that the Mitsubishi substrate was already wet or has absorbed as much water as it can. While the Mitsubishi substrate-based sensor leverages water absorption-induced conductivity changes, we encountered limitations when attempting to apply this concept to the bio-inspired membrane. Consequently, an alternative solution consisting of a sensor based on GO with Nafion was developed for the bio-inspired membrane. The composite was performed following the previously reported protocol (Yakoh et al., 2018) and as expected an exponential response was obtained (Fig. 4b), with the benefit that the resistance values were lower than those obtained for the interdigitated on Mitsubishi. Numerous humidity sensors exhibit sluggish responsiveness to humidity fluctuations due to the slow desorption of water from the sensor surface. However, one of the characteristics of heat stress is the absence of sweating, so having a fast-responding sensor is vitally important. To assess our sensor's reactivity, we conducted continuous resistance measurements while exposing the sensor to moist breath (Fig. 4c). The obtained results demonstrated the sensor's ability to restore its initial resistance value in less than a minute. The interesting feature of the Mitsubishi substrate trapping humidity may also be further exploited in a future work for the sensing and biosensing of metal ions and metabolites in sweat with appropriate normalization of the sweat rate (Yang et al., 2022; Rosati et al., 2018).

It is known the inherent temperature sensitivity of metals induces resistance changes, a phenomenon that extends to our humidity sensor crafted with silver ink. To mitigate this effect, temperature sensors of positive coefficient and negative coefficient were incorporated. The positive coefficient sensor consists of a silver-ink printed mender resistor, in the same way as the interdigitated one was printed. Silver traces are a porous material, exhibiting a resistivity approximately 10 times higher than bulk silver. Similarly, the thermal coefficient of the printed silver is different from its bulk counterpart. To quantify this, the resistor was exposed to various temperatures and its thermal coefficient was calculated using the equation $R = R_0 \cdot (1 + \alpha \Delta T)$. Our findings revealed that the alpha value for printed silver was $\alpha = 1.91 \cdot 10^{-3}$ (Fig. S4). Unlike metals, carbon-based materials such as rGO have a

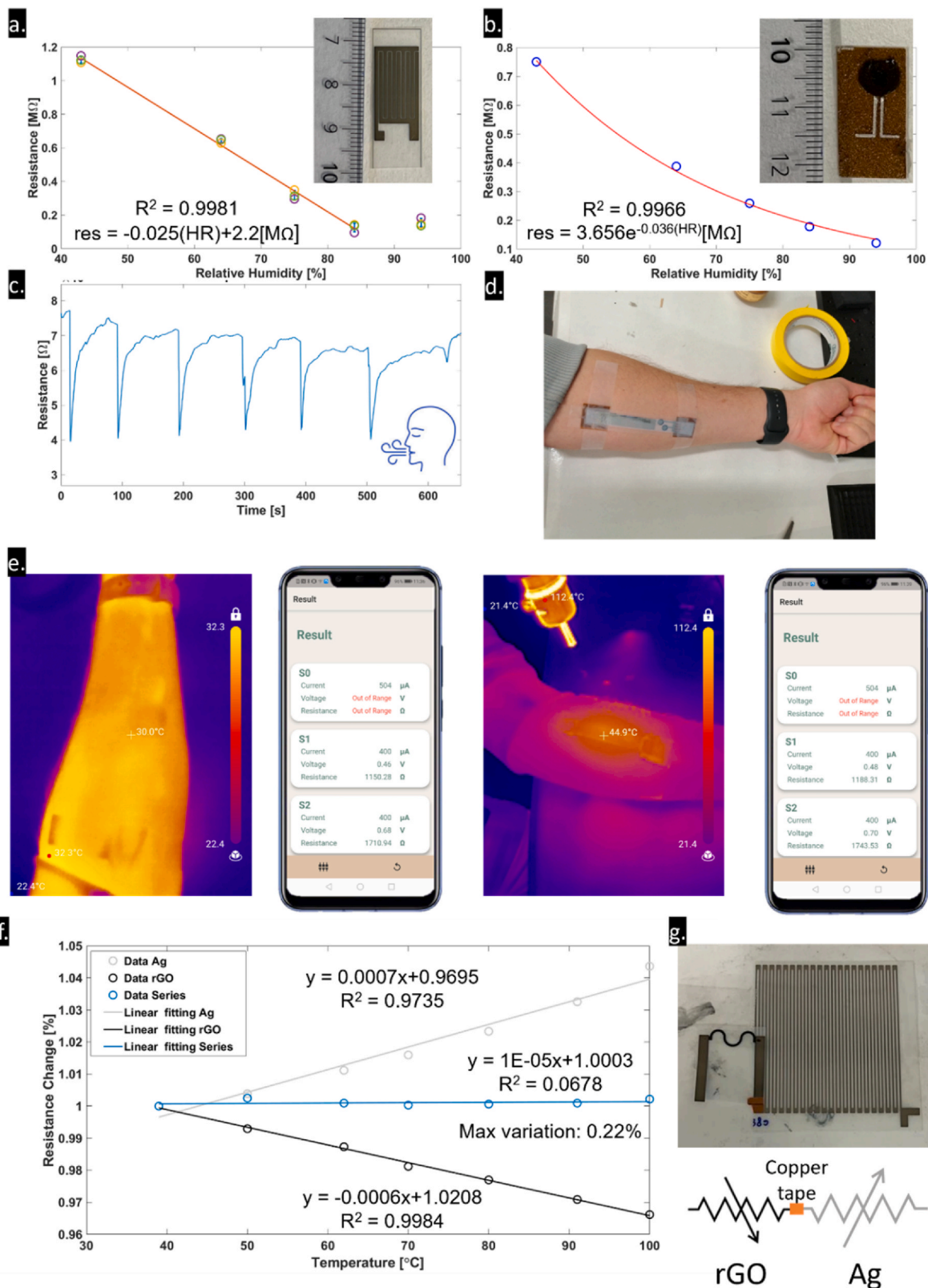


Fig. 4. a) Silver nanoparticles interdigitated electrode (IDE) humidity sensor inkjet-printed on semipermeable PET substrate. b) Comparison with a Nafion sensor on reduced graphene previously reported. c) Inkjet-printed humidity sensor response to breath and (d) illustration of the device positioning on skin for sweat detection and temperature sensing. e) Thermographs of the inkjet-printed device on the skin at room temperature and under hot air flushing for calibration. f) Calibration curves of the silver nanoparticles meander resistor and the rGO serpentine. g) Corresponding series of the two resistors.

negative thermal coefficient, which means that their resistance decreases as temperature rises. Fig. S4 shows different shapes of temperature sensors made with stamped rGO. From studying them at different temperatures, it was determined that their thermal coefficient is $\alpha = -5.8.10^{-4}$. These characteristics can be used to build flexible resistors that do not change their value with temperature. Fig. 4f and g show how by placing a silver printed resistor with a positive coefficient in series with a negative coefficient rGO stamped resistor it is possible to obtain a system whose resistance value becomes independent of temperature. In a practical temperature range (30–100 °C), the maximum recorded resistance variation was 0.22%. This negligible fluctuation renders our approach highly suitable for most applications. This innovative strategy was used in the construction of our wearable technology.

In our pursuit of effective wearable technology, we meticulously examine the performance of our sensors under real-world conditions. Specifically, we focused on temperature and humidity sensors, aiming to bridge the gap between laboratory-calibrated measurements and practical scenarios. For this, similar conditions to what a firefighter could be exposed to were mimicked, placing the sensor on the forearm and exposing it to hot air. Fig. 4e shows the thermal image of the arm with the sensor before and when exposed to heat as well as the values obtained with the smartphone by NFC. The initial value with the skin at 30 °C is 1150.28 Ω for sensor 1 (silver resistor), and 1710.94 Ω for sensor 2 (silver in series with rGO). After exposing the arm to the hot air, measurements were taken again obtaining 1188.31 Ω and 1743.53 Ω respectively. Taking the alpha values obtained during the characterization of the sensors, it is possible to estimate the temperature at:

$$T = \frac{R}{R_0} - 1 + T_0 = \frac{1188.31}{1150.28} - 1 + 30 = 47.33 \text{ } ^\circ\text{C}, \quad (\text{Eq. 2})$$

The rGO resistor value was determined by the difference between channel 1 and channel 2, as the resistors were in series. The obtained values are 560.66 Ω and 555.22 Ω , respectively. Applying again the equation Eq 2. the temperature obtained by this sensor is 46.73 °C.

The calculated temperatures closely align with those obtained using a thermal camera. In both measurements, it is observed that sensor 1 indicates 'Out of Range', which means that the skin is dry. In scenarios where the skin is wet, such as during physical activity, the sensor would yield a value, impacting the overall temperature sensor readings. Notably, the reported value would be lower due to the influence of humidity. The issue is evident in the *in vivo* tests presented in Fig. S5. To address this issue of sweat absorption and its interference with resistance measurements, the temperature sensor area was coated with wax, allowing for a protective layer to prevent unwanted moisture effects (Fig. S6). Sensor readings were taken during *in vivo* tests (Fig. S7) to capture the skin's temperature upon application, which was measured at 31 °C with the thermal camera. Interestingly, once the membrane secured the sensor in place, a cooling effect was observed due to its moisture content. This effect led to a decrease in temperature of 7° in both temperature sensors and a significant change in the humidity sensor value. This was evidenced by a decrease in sensor resistance values and confirmed by thermal imaging. As the person began to move, their body temperature gradually increased, resulting in a subsequent increase in sensor readings reflecting this physiological change. The recorded temperatures were approximately 13° higher, or around 6° above the initial baseline temperature (Table S1). These dynamic responses to physiological changes underscore the intricate interplay between sensor placement, environmental conditions, and user activity. In addition to the *in vivo* test, the real-time response of the temperature sensor powered by NFC can be seen in the SV2 video.

3.3. Muscle contraction simplified sensing

Surface myography, a critical tool for monitoring muscle activity, typically involves the placement of two electrodes along the muscle fibers, complemented by a third ground electrode in an unaffected zone

(generally near a joint). The resulting muscle action potential is then amplified and recorded over time with a sufficient sampling frequency to get all the information (typically with $f_s = 1$ KHz). Unfortunately, the conventional wired setup poses limitations, hindering natural movements, or requiring relatively bulky electronics next to the sensors. In our innovative approach, we repurpose the SIC4341 NFC chip, originally designed for simple electrochemical measurements (such as amperometry), to perform two-electrode recording of muscle action potentials.

The two electrodes were affixed to the skin utilizing conductive carbon tape. Notably, this tape exhibits a higher impedance compared to conventional conductive gels. However, these gels present two significant drawbacks for this specific application. Firstly, given the semi-permeable nature of our substrate, the gel tends to disperse across the substrate, thereby posing a risk of short-circuiting the electrodes. Secondly, these gels exhibit a capacitive response that can result in a phase shift of up to 40°. The gel behaves like a resistor-capacitor filter that enhances some frequencies and mitigates others, deforming the signal. In contrast, the carbon tape, while being tenfold more resistive than the gel, maintains a consistent value across varying frequencies and does not exhibit a capacitive component. A comparative analysis of these two connection modalities is presented in the tables and Figs. S8–S11.

The utilized setup enabled the direct quantification of currents linked to muscle contractions, facilitated by the NFC chip. This system, powered wirelessly, allowed for real-time, battery-free data acquisition via a smartphone. Despite the signal's limited frequency content owing to the device's relatively low sampling rate, and the signal's partial drift due to the lack of a ground electrode, the results shown in Fig. 5 unequivocally demonstrate the accurate detection of muscle contractions. We rigorously tested our system on various muscle groups. The testing was performed for the finger's extension muscles on the back of the forearm (Figure S12 and Fig. 5a) and for the triceps and biceps muscles in response to the extension (Fig. 5b) and contraction of the forearm (Fig. 5c), respectively. The red arrows denote the instances of action execution: finger movement, tricep contraction without load, and bicep contraction with load, respectively. Conversely, the light blue arrows represent the resting positions: fingers curled into a relaxed fist without exerting force, the tricep relaxed without weight resistance, and the extended arm position during the bicep exercise involving weightlifting (Fig. S13–S14). The results found so far prove that the system could be used for the detection of seizures, if accurately placed, which are a possible effect of heat stroke.

3.4. Direct printing on the membrane and advantages and disadvantages of inkjet and Voltera printing

Aiming for efficient wearable antennas, we encountered critical challenges during the fabrication process. Two different approaches were explored for printing the antenna on the bio-inspired membrane. Specifically, we investigated inkjet printing techniques and the capabilities of a Dimatix (Fujifilms DMP 2800 series) research-grade printer. Initially, an exploration into inkjet printing techniques was conducted, using an Epson XP15000 Consumer Printer (Fig. S15). However, a critical challenge emerged with the inherent need for these materials to be dry, resulting in their increased brittleness and fragility. The inherent risk to the printer's internal components, particularly the rollers and paper drive wheels, prompted us to seek alternative solutions. To mitigate this risk, we utilized the CD printing tool provided with the printer, allowing the substrate to remain flat with minimal movement. Nonetheless, this method presents a drawback: unlike conventional printing software that enables adjusting print quality based on Dots Per Inch (DPI) settings, the CD tool necessitates an image file. However, this image is compressed, resulting in significantly lower quality and compromised conductivity due to reduced deposition of silver ink. This limitation adversely impacts the final print quality. Although it was possible to print some patterns, printing with silver ink requires a

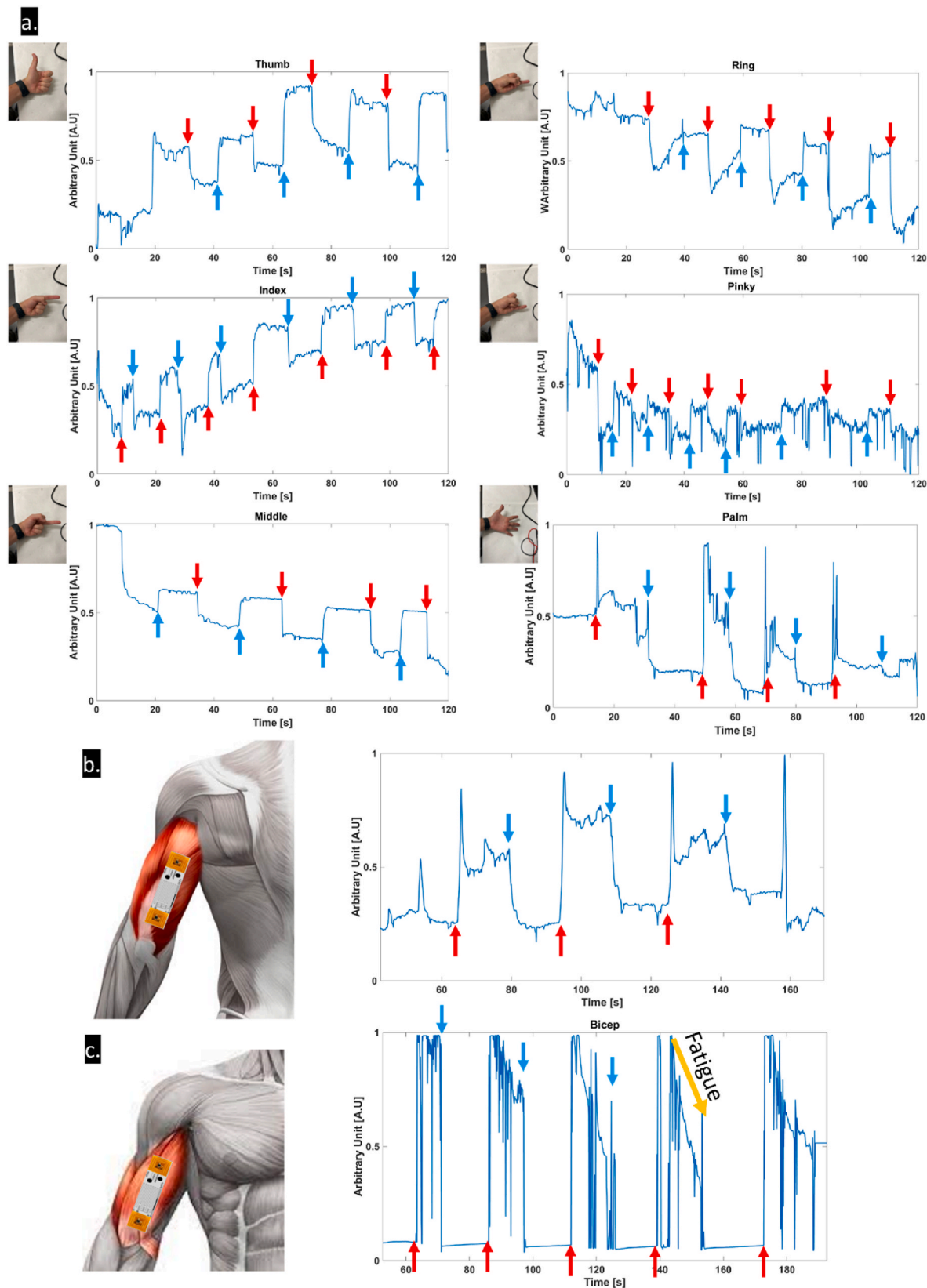


Fig. 5. a) Simplified surface electromyography (ssEMG) normalized measurement on the forearm for the detection of the fingers muscle contraction. b) SsEMG normalized measurements on the tricep muscle and (c) on the bicep muscle. The red arrows indicate the contraction and the blue ones the rest phases in all the plots.

subsequent sintering process at high temperatures to make the tracks conductive (Fig. S16) (Maroli et al., 2023). Regrettably, this process damaged the membranes and permanently adhered them to the CDs used as holders.

Having ruled out consumer printing, we explored the Dimatix (Fujifilm DMP 2800 series) printer. Among other parameters, this research-grade printer offers adjustable drop spacing and platform temperature during printing. In this case, we were able to print a functional antenna on the membrane, as shown in Fig. S17. However, this process proved tedious and time-consuming. To prevent any short circuits between antenna tracks, we restricted printing to a single nozzle. Additionally, to achieve good conductivity it was still necessary to apply the thermal sintering process, so it was not possible to remove the membrane from the sacrificial substrate, in this case PET, after the sintering process. It is for this last reason that the inkjet printing approach was discarded for printing directly on the membrane. Instead, a V-One printer from Voltera was used, which is a paste dispenser instead of

printing inks. Printing with this system has two major advantages, the first is that the substrate is kept flat on a surface while the carriage that extrudes the silver paste moves over it. On the other hand, silver pastes, in addition to not requiring a sintering process, form a thicker and thus more conductive layer (Figs. S18 and S19 present SEM images of the printed traces), so it has been possible to design a smaller antenna than the one printed with inkjet ink. Resistance and inductance measurements of the Voltera printed antenna are shown in Fig. S20 and Fig. S21.

As shown in Fig. 6, the bio-inspired membrane was placed in a container with water and carefully lifted with a piece of PET. Next, the PET with the membrane is placed in the Voltera V-One, where the desired design loaded through the Gerber files was printed using silver paste. Once the antenna and contact pads were printed, the SIC-434X chip was placed. Due to the size of the chip pad, it was not easy to solder it directly onto the substrate. To overcome this limitation, we designed a small auxiliary PCB (25 mm long by 8 mm wide) to serve as an adapter. This auxiliary PCB not only facilitated chip attachment but

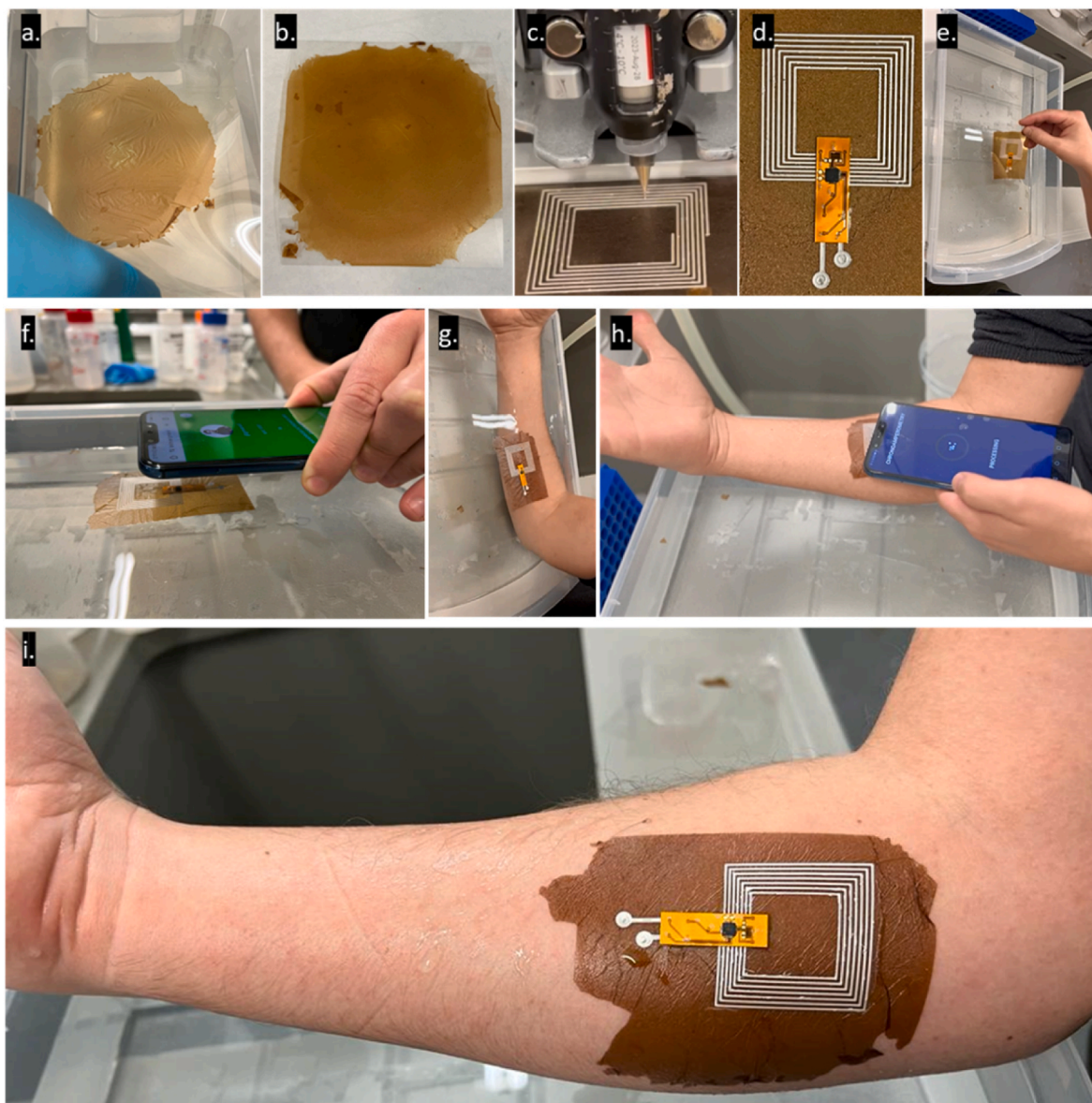


Fig. 6. Pictures of the fabrication phases of the printed sensorised bioadhesive membranes. a) Free-standing membrane on water. b) Transfer on the plastic temporary substrate for printing. c) Silver paste deposition with Voltera equipment to form the NFC antenna. d) Attachment of the flexible PCB integrating the NFC chip on the printed membrane. e) Release of the printed membrane from the temporary substrate. f) Testing of the NFC connection on the free-standing membrane on water. g) Adhesion of the membrane to the forearm skin. h) Testing of the NFC connection on the adhered membrane. i) Close-up of the printed membrane. The membrane has been placed with the antenna, chip and ssEMG contacts on top only for illustrative purposes.

also allowed for removal after device use. Moreover, it enabled reuse in new devices, employing Electrically Conductive Adhesive Transfer Tape (ECATT). This PCB was manufactured in flexible polyamide substrate, by the company PCB-Way (Fig. S22). The chip was soldered onto the PCB using Voltera's solder paste and then the flexible PCB and chip assembly were stuck to the membrane by employing a unique piece of ECATT, specifically the 3M Electrically Conductive Adhesive Transfer Tape 9703. This ECATT boasts anisotropic electrical conductivity, meaning it facilitates current flow exclusively through the thickness of the adhesive ('Z-axis') and not along its plane. This selective conductivity was achieved by embedding the adhesive matrix with conductive particles positioned to create point-to-point connections across the adhesive layer while maintaining electrical insulation laterally. This characteristic is particularly advantageous in preventing short circuits among the closely spaced pads and ensures reliable, targeted electrical connections. In order to detach the device from the PET, the device was again immersed tangentially in water (Fig. 6e). The system was then tested in water to verify that the membrane has not broken or that the PCB had not detached on contact with water (Fig. 6f). Next, the arm was then immersed in the water tank and the membrane stuck to the arm as it was taken out from the tank (Fig. 6g). Finally, the smartphone was brought close to the device for reading via NFC (Fig. 6h). All the steps of this process can be seen in detail in the [Supplementary Information video SV3](#).

4. Conclusions

In this work, we have introduced a novel compact layout for an inkjet-printed wearable capable of measuring temperature, humidity (sweating), and muscle contractions. Crucially, this wearable can be powered and read with a smartphone via wireless NFC. Beyond this, we demonstrated the use of this methodology for the integration of sensors in bio-inspired and conformable membranes that imitates water-resistant adhesion observed in mussels. We have compared approaches of printing the sensors and antennas for the NFC readout on the membranes by inkjet printing and by the deposition of pastes using a Voltera printer, outlining the advantages and disadvantages of each strategy.

We have accurately designed the sensor network to reach the highest possible grade of integration for this type of fabrication method. In fact, we have: i) addressed the limitations of temperature sensing via a meander resistor by introducing an additional reduced graphene oxide resistor to compensate for the resistance change effect induced by bending, strain, or humidity variations; ii) taken advantage of the absorbent coating of the plastic substrate used for inkjet printing, enhancing humidity sensing with resistive IDE and iii) used simple amperometric measurements to measure the current associated with the muscle action potential, enabling surface electromyographic envelope identification related to muscle contraction. Finally, we have validated all the sensors with both laboratory-based and *in vivo* testing on a healthy volunteer performing physical exercise. This ensures the platform's reliability, effectively bridging the gap between wearability and precise monitoring.

All in all, these devices may become an important point for the prevention of life-risk emergency conditions such as both classic and exertional heat stroke. The multi-sensing capability and appropriate normalization algorithms, wireless connectivity and real-time connection, and natural movement compatibility are essential features of these prevention systems. Future directions will be focused on long-term reliability, robustness of such complex systems and cross-interference reduction remain critical areas for further exploration.

CRedit authorship contribution statement

Gabriel Maroli: Writing – review & editing, Writing – original draft, Methodology, Investigation, Formal analysis, Data curation, Conceptualization. **Giulio Rosati:** Writing – review & editing, Writing – original

draft, Supervision, Funding acquisition, Conceptualization. **Salvio Suárez-García:** Writing – review & editing, Writing – original draft, Supervision, Project administration, Conceptualization. **Daniel Bedmar-Romero:** Methodology, Investigation. **Robert Kobrin:** Writing – review & editing, Methodology, Investigation. **Álvaro González-Laredo:** Methodology, Investigation. **Massimo Urban:** Methodology, Investigation. **Ruslan Álvarez-Diduk:** Writing – review & editing, Supervision. **Daniel Ruiz-Molina:** Writing – review & editing, Supervision, Resources, Funding acquisition. **Arben Merkoçi:** Supervision, Resources, Funding acquisition.

Declaration of competing interest

The authors declare that they have no known competing financial interests or personal relationships that could have appeared to influence the work reported in this paper.

Data availability

Data will be made available on request.

Acknowledgments

The ICN2 is funded by the CERCA programme/Generalitat de Catalunya. The ICN2 has been supported by the Severo Ochoa Centres of Excellence programme [SEV-2017-0706] and is currently supported by the Severo Ochoa Centres of Excellence programme, Grant CEX2021-001214-S, both funded by MICIU/AEI/10.13039/501100011033. The MiaSkin project has been funded by the ICN2 Severo Ochoa Seed Funding for Emerging Topics 2021 Program. This project has received funding from the European Union's Horizon 2020 research and innovation programme under grant agreement No 101008701. Views and opinions expressed are however those of the author(s) only and do not necessarily reflect those of the European Union. The European Union can not be held responsible for them. We acknowledge Departament de Recerca i Universitats of Generalitat de Catalunya for the grant 2021 SGR 01464. This work was supported by grants PID2021-124795NB-I00 and PID2021-127983OB-C21 financed by MICIU/AEI/10.13039/501100011033 and ERDF "A way to make Europe". G.M. would like to express his gratitude to the Carolina Foundation for financial support through the scholarship "Doctorado 2020". G.M. acknowledges Universitat Autònoma de Barcelona (UAB) for the possibility of performing this work inside the framework of Chemistry PhD Programme. G.M. thanks Patricia Batista Deroco and Lei Zaho for their advice on the Dimatix printer. G.M. thanks Nerea de Mariscal i Molinas for her help in filming the S.I. video.

Appendix A. Supplementary data

Supplementary data to this article can be found online at <https://doi.org/10.1016/j.bios.2024.116421>.

References

- Al Mahri, S., Bouchama, A., 2018. Chapter 32 – heatstroke. In: Romanovsky, A.A. (Ed.), *Handbook of Clinical Neurology*, vol. 157. Elsevier, pp. 531–545.
- Barmpakos, D., et al., 2020. *Microelectron. Eng.* 225, 111266.
- Barros, N.R., et al., 2021. *Biomater. Sci.* 9, 6653–6672.
- Baumgartner, C., et al., 2021. *Seizure. Eur. J. Epilepsy* 86, 52–59.
- Chen, S.-T., et al., 2017. *Sensors* 18, 17.
- Conradsen, I., et al., 2011. *Annu. Int. Conf. IEEE Eng. Med. Biol. Soc.* 7715–7718.
- Contreras-Pereda, N., et al., 2024. *Mater. Today Chem.* 35, 101855.
- Djmal, A., et al., 2023. *Bioengineering* 10, 703.
- Ershad, F., et al., 2020. *Nat. Commun.* 11, 3823.
- Haerinia, M., Noghianian, S., 2019. *Sensors* 19, 1732.
- Ju, J., et al., 2022. *ACS Appl. Mater. Interfaces* 14, 25115–25125.
- Kim, S., et al., 2019. *Ind. Health* 57, 370–380.
- Laitano, O., et al., 2019. *J. Appl. Physiol.* 127, 1338–1348.
- Lee, H., et al., 2006. *Proc. Natl. Acad. Sci. USA* 103, 12999–13003.

- Maroli, G., et al., 2021. Arg. Conf. on Electr. (CAE) 61–66.
- Maroli, G., et al., 2023. Arg. Conf. on Electr. (CAE) 69–74.
- Maroli, G., et al., 2023. Front. Electron. 3, 1060197.
- Matsumoto, K., et al., 2019. 41st Ann. Int. Conf. Of the IEEE Eng. In: Med. And Biol. Soc. EMBC, pp. 7049–7055.
- McEntire, S.J., et al., 2013. Prehosp. Emerg. Care 17, 241–260.
- Momose, H., et al., 2023. Sci. Rep. 13, 416.
- Nalepa, M., et al., 2024. Biosens. Bioelectron. 256, 116277.
- Pham, S., et al., 2020. Sensors 20, 855.
- Rosati, G., et al., 2022. Biosens. Bioelectron. 196, 113737.
- Rosati, G., et al., 2021. Sci. Rep. 11, 14938.
- Rosati, G., et al., 2018. Biosens. Bioelectron. 21, 54–64.
- Rossetti, M., et al., 2024. Biosens. Bioelectron. 250, 116079.
- Saiz-Poseu, J., et al., 2019. Angew. Chem. Int. 58, 696–714.
- Scroccarello, A., et al., 2023. ACS Sens. 8, 598–609.
- Shimazaki, T., et al., 2022. Sensors 22, 395.
- Suárez-García, S., et al., 2017. Biomimetics 2, 22.
- Sousa, M.P., et al., 2018. Biomater. Sci. 6, 1962–1975.
- Yakoh, A., et al., 2018. ACS Appl. Mater. Interfaces 10 (24), 20775–20782.
- Yang, Q., et al., 2022. Biosens. Bioelectron. 202, 114005.
- Zhao, L., et al., 2023. ACS Appl. Mater. Interfaces 15, 9024–9033.